Computational Methods for Continuum Models of Platelet Aggregation

Nien-Tzu Wang and Aaron L. Fogelson

Department of Mathematics, University of Utah, Salt Lake City, Utah 84112
E-mail: nwang@math.utah.edu, fogelson@math.utah.edu

Platelet aggregation plays an important role in blood clotting. Robust numerical methods for simulating the behavior of Fogelson's continuum models of platelet aggregation have been developed which in particular involve a hybrid finite-difference and spectral method for the models' link evolution equation. This partial differential equation involves *four* spatial dimensions and time. The new methods are used to begin investigating the influence of new chemically induced activation, link formation, and shear-induced link breaking in determining when aggregates develop sufficient strength to remain intact and when they are broken apart by fluid stresses. © 1999 Academic Press

Key Words: platelet aggregation; continuum models; computational fluid dynamics; spectral methods; high-resolution advection algorithm; immersed boundary method.

1. INTRODUCTION

The aggregation of blood platelets is one of the first steps in thrombosis and normal hemostasis. It can contribute to prevention of excessive blood loss when a blood vessel is injured, and it can also result in occlusive arterial diseases. In particular, abnormal platelet aggregation in the coronary arteries can limit the blood flow to the heart muscle, thus leading to cardiac ischemia, life-threatening arrhythmias, and myocardial necrosis [24]. This work concerns the development of numerical methods for studying mathematical models of platelet aggregation in vessels the size of the coronary arteries or larger.

Under normal conditions, platelets circulate in the blood flow with a disc shape and in a nonadherent state. However, when a blood vessel wall is damaged by injury or disease, a variety of platelet-reactive substances, most noteworthy of which are the collagens, are exposed to the blood. Circulating platelets that contact the damaged wall may be induced to begin an activation process in which (1) the platelets change shape to a spherical spiny cell, and then release chemicals into blood which can activate other platelets; (2) the membranes

of the platelets become sticky and capable of adhesion with other activated platelets. If the process is functioning correctly, a platelet plug forms at the injury site. Many clinical results indicate that a deficiency in circulating platelets is associated with "spontaneous" hemorrhages from small vessels. Platelets are hence thought to have an important role in maintaining the functional integrity of these vessels [6].

The dense granules in the platelet cytoplasm contain a number of chemicals, which are secreted into the surrounding fluid when the platelet is activated. One of these released chemicals, ADP, is thought to be the primary nucleotide that causes platelet aggregation in physiological situations [22]. For human platelets, ADP can induce different events depending on its concentration. In a stirred suspension of platelets, ADP at low concentrations induces reversible aggregation, while sufficiently high concentrations of ADP induce irreversible aggregation as well as the secretion of additional ADP by the platelets [15].

Platelets and activating chemicals are carried by the moving fluid. Exposure of platelets to high enough levels of chemical activate them, causing them to release more chemical and priming them to cohere. The growth of platelet aggregates as platelets adhere to the damaged vessel wall and to one another disturbs the local fluid motion, sometimes profoundly, and this completes the cycle of coupling among platelets, fluid, and chemical.

Fogelson's continuum models of platelet aggregation [11, 12] describe interactions among a viscous, incompressible fluid with velocity $\mathbf{u}(\mathbf{x}, t)$ and pressure $p(\mathbf{x}, t)$; populations of nonactivated and activated platelets with densities $\phi_n(\mathbf{x}, t)$ and $\phi_a(\mathbf{x}, t)$, respectively; a distribution of interplatelet bonds with density $E(\mathbf{x}, \mathbf{v}, t)$; and the activating chemical ADP with concentration $c(\mathbf{x}, t)$. The models involve two distinct length scales: the diameter of a coronary artery is on the order of 1–2 mm, and the diameter of a platelet is about 2 μm. Therefore, two sets of spatial variables appear in the models. These are $\mathbf{x}$ and $\mathbf{v}$ for which the statements $|\mathbf{x}| = O(1)$ and $|\mathbf{v}| = O(1)$ indicate lengths comparable to a vessel diameter and platelet diameter, respectively. The ratio of platelet diameter to vessel diameter is denoted by ϵ, and $\epsilon \ll 1$. The equations of the continuum models are derived in the limit that $\epsilon \to 0$.

A general form of the models involves the equations

$$\rho(\mathbf{u}_t + \mathbf{u} \cdot \nabla \mathbf{u}) = -\nabla p + \mu \Delta \mathbf{u} + \mathbf{f}^g + \mathbf{f}^p, \tag{1}$$

$$\nabla \cdot \mathbf{u} = 0, \tag{2}$$

$$\frac{\partial \phi_n}{\partial t} + \mathbf{u} \cdot \nabla \phi_n = D_n \Delta \phi_n - R(c)\phi_n, \tag{3}$$

$$\frac{\partial \phi_a}{\partial t} + \mathbf{u} \cdot \nabla \phi_a = R(c)\phi_n, \tag{4}$$

$$\frac{\partial c}{\partial t} + \mathbf{u} \cdot \nabla c = D_c \Delta c + A R(c)\phi_n, \tag{5}$$

$$E_t + \mathbf{u} \cdot \nabla_{\mathbf{x}} E + (\mathbf{v} \cdot \nabla \mathbf{u}) \cdot \nabla_{\mathbf{v}} E = \alpha(|\mathbf{v}|)\phi_a^2 - \beta(|\mathbf{v}|)E, \tag{6}$$

$$\mathbf{f}^p(\mathbf{x}, t) = \frac{1}{2} \int \mathbf{v} \cdot \nabla_{\mathbf{x}} E(\mathbf{x}, \mathbf{v}, t) S(|\mathbf{v}|)\mathbf{v} \, d\mathbf{v}. \tag{7}$$

The motion of the fluid is described by the incompressible Navier–Stokes equations (1) and (2) with constant density ρ and viscosity μ. There are two force density terms in Eq. (1): $\mathbf{f}^g$ is a given force density to drive a background flow, and $\mathbf{f}^p$, called the cohesion-force density, is produced by the interplatelet bonds between activated platelets.

Equations (3)–(5) concern changes in the platelet densities and the concentration of ADP. Each of these is transported by advection with velocity **u** and by diffusion. The diffusive motion of platelets is due to local flow disturbances induced by the tumbling red blood cells. We expect that the influence of this motion on activated platelets within an aggregate is less than that on single nonactivated platelets. For simplicity, the activated platelets are assumed to have no diffusive motion. When platelets are activated, the density of nonactivated platelets decreases at the rate $R(c)\phi_n$, and the activated platelet density increases at the same rate. There is a corresponding production of ADP at a rate $AR(c)\phi_n$, where A is the amount of ADP secreted by a single platelet.

The evolution of the density of interplatelet bonds $E(\mathbf{x}, \mathbf{v}, t)$ is described in Eq. (6). E is a function of time t, the usual spatial coordinates $\mathbf{x}$, as well as the (scaled) vector $\mathbf{v}$ that represents the connection between two ends of an interplatelet bond. E is advected at velocity $\mathbf{u}$ in $\mathbf{x}$-space and at velocity $(\mathbf{v} \cdot \nabla \mathbf{u})$ in $\mathbf{v}$-space. The latter term is due to the difference in velocity $\mathbf{u}$ at the two ends of an interplatelet bond. The right hand side of Eq. (6) states that new bonds are created at the rate $\alpha(|\mathbf{v}|)\phi_a^2$, and that existing bonds are broken at the rate $\beta(|\mathbf{v}|)E$. Equation (7) gives the cohesion-force density in terms of an integral over all of $\mathbf{v}$-space with the integrand involving ∇E and the force $S(|\mathbf{v}|)\mathbf{v}$ generated by a single bond of length $|\mathbf{v}|$ and direction $\mathbf{v}/|\mathbf{v}|$. Detailed derivations of Eqs. (6)–(7) can be found in [11].

We can also define the cohesion-stress *tensor* $\underline{\underline{\sigma}}^p(\mathbf{x}, t)$ by the formula

$$\underline{\underline{\sigma}}^p(\mathbf{x}, t) = \frac{1}{2} \int E(\mathbf{x}, \mathbf{v}, t) S(|\mathbf{v}|)\mathbf{v}\mathbf{v}^T \, d\mathbf{v}. \tag{8}$$

If we know $\underline{\underline{\sigma}}^p$, then we can obtain the cohesion-force density $\mathbf{f}^p$ as its divergence

$$\mathbf{f}^p = \nabla \cdot \underline{\underline{\sigma}}^p. \tag{9}$$

In Eq. (6), α and β are the rate functions for creating and breaking interplatelet bonds, respectively, and both are dependent on the bond length $|\mathbf{v}|$. In the special case that $\beta(|\mathbf{v}|) = \beta_0$ is a constant independent of $|\mathbf{v}|$, and under the additional assumption that each bond breaks with a linear spring with zero resting length ($S(|\mathbf{v}|) = k_0$), then a transport equation for $\underline{\underline{\sigma}}^p$ can be derived (see [11])

$$\underline{\underline{\sigma}}^p_t + \mathbf{u} \cdot \nabla \underline{\underline{\sigma}}^p = \underline{\underline{\sigma}}^p \underline{\nabla \mathbf{u}} + (\underline{\underline{\sigma}}^p \underline{\nabla \mathbf{u}})^T + a_2 \phi_a^2 \underline{\underline{I}} - \beta_0 \underline{\underline{\sigma}}^p, \tag{10}$$

which is a 2-dimensional partial differential equation. In this special case, we can use Eqs. (9)–(10) in place of Eqs. (6)–(7), and since all reference to $\mathbf{v}$ drops out, computing the models' solution is much less costly than for the general form of the models. The special case of the platelet aggregation models was studied computationally by Fogelson in [11, 12].

In this paper, we are concerned with developing numerical methods for studying, in two dimensions, the general form of the aggregation models given by Eqs. (1)–(7). The general form requires solving the *four-dimensional* partial differential equation (6) and integrating over $\mathbf{v}$-space to compute the cohesion force density $\mathbf{f}^p$ at each point $\mathbf{x}$ according to the formula (7). The motivation for wanting to study the general form of the models is that only it permits the interplatelet bonds to be sensitive to strain within an aggregate; Eq. (6) allows us to study both a strain-dependent bond breaking rate $\beta(|\mathbf{v}|)$ and a bond force which depends nonlinearly on the strain $|\mathbf{v}|$.

Equation (6) is a partial differential equation which involves time and four independent spatial variables. It is the most challenging part of the models to solve. To make it more tractable, we transform the $\mathbf{v}$-plane in (6) into polar coordinates (r, θ) and use spectral methods to take advantage of E's periodicity in θ. The term $(\mathbf{v} \cdot \nabla \mathbf{u}) \cdot \nabla_{\mathbf{v}} E$ in (6), which describes convection of E in $\mathbf{v}$-space at "velocity" $(\mathbf{v} \cdot \nabla \mathbf{u})$, is the only nontrivial term to transform. After some algebra, we find that

$$(\mathbf{v} \cdot \nabla \mathbf{u}) \cdot \nabla_{\mathbf{v}} E = r p(\theta) E_r(\mathbf{x}, r, \theta, t) + q(\theta) E_\theta(\mathbf{x}, r, \theta, t),$$

where

$$p(\theta) = u_x \cos^2 \theta + (v_x + u_y) \sin \theta \cos \theta + v_y \sin^2 \theta,$$

and

$$q(\theta) = v_x \cos^2 \theta + (-u_x + v_y) \sin \theta \cos \theta - u_y \sin^2 \theta.$$

Both p and q depend on the first partial derivatives of the components of $\mathbf{u}$ and have the property that $2p(\theta) + q'(\theta) = 0$. This is a consequence of the incompressibility of the velocity $\mathbf{u}$. Now, Eq. (6) becomes

$$E_t(\mathbf{x}, r, \theta, t) + \mathbf{u} \cdot \nabla_{\mathbf{x}} E(\mathbf{x}, r, \theta, t) + r p(\theta) E_r(\mathbf{x}, r, \theta, t) + q(\theta) E_\theta(\mathbf{x}, r, \theta, t)$$
$$= \alpha(r) \phi_a^2(\mathbf{x}, t) - \beta(r) E(\mathbf{x}, r, \theta, t). \tag{11}$$

We also rewrite the cohesion force formula (7) in polar coordinates as

$$
\begin{aligned}
\mathbf{f}^p(\mathbf{x}, t) &= \frac{1}{2} \int_0^{\bar{r}} \int_0^{2\pi} \mathbf{v}(r, \theta) \cdot \mathbf{g}(\mathbf{x}, r, \theta, t) S(r) \mathbf{v}(r, \theta) r \, d\theta \, dr \\
&= \frac{1}{2} \int_0^{\bar{r}} \int_0^{2\pi} (r \cos \theta g_1 + r \sin \theta g_2) \begin{pmatrix} r \cos \theta \\ r \sin \theta \end{pmatrix} S(r) r \, d\theta \, dr \\
&\stackrel{\pi-\text{periodic}}{=} \int_0^{\bar{r}} \int_0^{\pi} \begin{pmatrix} \cos^2 \theta g_1 + \sin \theta \cos \theta g_2 \\ \sin \theta \cos \theta g_1 + \sin^2 \theta g_2 \end{pmatrix} S(r) r^3 \, d\theta \, dr, \tag{12}
\end{aligned}
$$

where $\mathbf{g}(\mathbf{x}, r, \theta, t) = \nabla_{\mathbf{x}} E(\mathbf{x}, r, \theta, t)$, and we truncate the r-integration at $r = \bar{r} = O(1)$ because E is negligibly small for $r \gg 1$ (see [11]).

The numerical method we developed makes use of high-resolution finite difference schemes originally developed for nonlinear conservation laws [20] and of Fourier spectral methods [7, 13]. Therefore, Section 2 presents a hybrid algorithm combining a spectral method and finite-difference scheme. A special case is tested and the algorithm is shown to be numerically second order accurate. A brief description of the advection scheme is given in Section 3. A numerical algorithm for a partial differential equation with four spatial variables is tested in Section 4. This is preparation for solving the full continuum models. Section 5 describes the numerical methods for the full continuum model as well as the design and results of a series of numerical experiments on the full model. It also describes experiments which use the new numerical methods to examine the mechanical properties of the platelet aggregate composite material. Finally, Section 6 contains the conclusions and plans for future work.

2. HYBRID SCHEME FOR THE TWO-DIMENSIONAL MODEL PROBLEM

In this section we consider numerical methods for equations that model the **v**-dependent terms in the evolution equation (11) for the density of interplatelet bonds E. Recall that when polar coordinates are used to describe the **v**-plane, this equation contains terms of the form $rp(\theta)E_r$ and $q(\theta)E_\theta$ where the functions $p(\theta)$ and $q(\theta)$ satisfy the constraint $2p(\theta) + q'(\theta) = 0$.

We consider the model equation

$$f_t + rp(\theta)f_r + q(\theta)f_\theta = 0 \tag{13}$$

$$f(r, \theta, 0) = g(r, \theta)$$

in the domain $0 \le r \le 1, 0 \le \theta < 2\pi$. We are interested in the case that $p(\theta)$, $q(\theta)$, and $g(r, \theta)$ are π-periodic in θ, and then $f(r, \theta, t)$ is easily seen to be π-periodic as well. Hence, it suffices to consider $0 \le \theta < \pi$.

We discretize the θ-interval $[0, \pi)$ using the nodes, $\theta_j = \frac{j\pi}{N}$, $j = 0, \ldots, N - 1$, and we discretize the r-interval $[0, 1]$ using the points $r_i = \frac{i}{M}$, $i = 0, \ldots, M$. The notation $f_{i,j}^n$ denotes the value of the numerical solution at time $t = n\Delta t$, at $\theta = \theta_j = \frac{j\pi}{N}$, and at the center of the ith cell $[r_i - \frac{1}{2M}, r_i + \frac{1}{2M}]$. The layout of cells is shown in Fig. 1.

We approximate the term f_θ using a spectral method [7, 13]. For us, the benefit of this method is not the extraordinary accuracy available for large N but rather the small size of N necessary for a moderately accurate solution. The approximate derivative $[D_\theta f(r, \theta, t)]$ is defined as

$$[D_\theta f(r, \theta, t)]_j = \sum_{k=-N/2}^{N/2-1} a_k e^{ik\theta_j}, \qquad j = 0, 1, \ldots, N - 1,$$

where

$$a_k = \begin{cases} \frac{ik}{N} \sum_{l=0}^{N-1} f(r, \theta_l, t)e^{-ik\theta_l}, & \text{if } k = -N/2 - 1, \ldots, N/2 - 1, \\ 0, & \text{if } k = -N/2. \end{cases}$$

This is called the Fourier collocation derivative of the function $f(r, \theta, t)$, based on the collocation points $\{\theta_j\}$. To calculate the collocation derivative, one calculates the coefficients
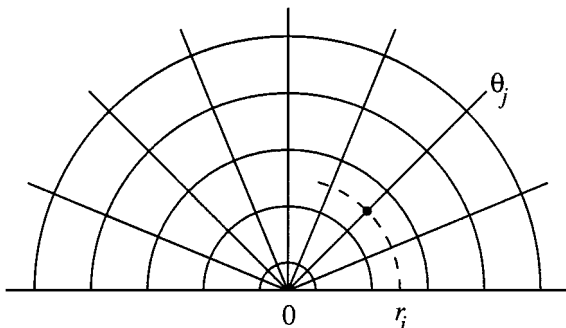
FIG. 1. Cells in polar coordinates.

of the discrete Fourier transform of f, multiplies the kth coefficient by ik for each k, then transforms the resulting Fourier coefficients back to physical space using the inverse Fourier transform. A reason for using a collocation approach is that it can be applied to a variable coefficient problem, and Fourier series are appropriate for problems with periodic boundary conditions.

To approximate the $rp(\theta)f_r$ term, we adapt the approach of Bell and Marcus [1], which in turn was motivated by Colella's multidimensional upwind schemes for nonlinear conservation laws [9]. To begin, f is extrapolated to the left side of edge $r = r_i + \frac{1}{2M}$ of cell i at time $t^{n+1/2}$ using

$$f_{i,j}^n + \frac{\Delta r}{2}\left(\frac{\partial f}{\partial r}\right)_{i,j}^n + \frac{\Delta t}{2}\left(\frac{\partial f}{\partial t}\right)_{i,j}^n = f_{i,j}^n + \frac{\Delta r}{2}\left(\frac{\partial f}{\partial r}\right)_{i,j}^n + \frac{\Delta t}{2}\left[-rp(\theta)\frac{\partial f}{\partial r} - q(\theta)\frac{\partial f}{\partial \theta}\right]_{i,j}^n.$$

The partial differential equation was used to replace $\frac{\partial f}{\partial t}$ by spatial derivatives of f. Upon approximating the spatial derivatives, we obtain the approximate mid-time edge value

$$f_{i+1/2,j}^{n+1/2,L} = f_{i,j}^n + \frac{1}{2}[\Delta r - \Delta t r_i p(\theta_j)](f_r^n)_{i,j} - \frac{\Delta t}{2}q(\theta_j)[D_\theta f^n]_{i,j}.$$

Similarly, f is extrapolated to the right side of edge $r = r_{i+1} - \frac{1}{2M} = r_i + \frac{1}{2M}$ of cell $(i+1)$ to give

$$f_{i+1/2,j}^{n+1/2,R} = f_{i+1,j}^n - \frac{1}{2}[\Delta r + \Delta t r_{i+1} p(\theta_j)](f_r^n)_{i+1,j} - \frac{\Delta t}{2}q(\theta_j)[D_\theta f^n]_{i+1,j}.$$

Here

$$(f_r^n)_{i,j} = \frac{(\Delta^r f^n)_{i,j}}{\Delta r},$$

where

$$(\Delta^r f^n)_{i,j} = \begin{cases} \min\left\{\frac{1}{2}\left|f_{i+1,j}^n - f_{i-1,j}^n\right|, 2\left|f_{i+1,j}^n - f_{i,j}^n\right|, 2\left|f_{i,j}^n - f_{i-1,j}^n\right|\right\} \\ \quad \times sgn(f_{i+1,j}^n - f_{i-1,j}^n), \qquad \text{if } (f_{i+1,j}^n - f_{i,j}^n)(f_{i,j}^n - f_{i-1,j}^n) > 0, \\ 0 \qquad\qquad\qquad\qquad\qquad \text{otherwise.} \end{cases}$$

That is, these are limited approximations to the r-derivatives at the r-edges of each cell. Next, the choice of edge values of f is resolved by solving a Riemann problem, i.e.,

$$f_{i+1/2,j}^{n+1/2} = \begin{cases} f_{i+1/2,j}^{n+1/2,L}, & \text{if } p(\theta_j) > 0, \\ f_{i+1/2,j}^{n+1/2,R}, & \text{if } p(\theta_j) < 0, \\ \frac{1}{2}\left(f_{i+1/2,j}^{n+1/2,L} + f_{i+1/2,j}^{n+1/2,R}\right), & \text{if } p(\theta_j) = 0. \end{cases}$$

Then, the edge values are used in a difference approximation to f_r:

$$(rpf_r)_{i,j}^{n+1/2} = r_i p(\theta_j)\frac{f_{i+1/2,j}^{n+1/2} - f_{i-1/2,j}^{n+1/2}}{\Delta r}. \tag{14}$$

In most applications of spectral methods to partial differential equations the spatial discretization is spectral but the temporal discretization is based on finite-differences. Many standard numerical time discretization schemes [16] can be applied, including, for example, the Runge–Kutta methods, the Leap-Frog method, the Adams–Bashforth methods, and so on. The choice of time discretization scheme influences the accuracy, stability, storage requirements, and work demands of the methods. In particular, the stability for a given problem is connected with the spectrum of the spatial discretization.

The stability region of the third-order Adams–Bashforth (AB3) method applied to the linear model problem ($u_t = \lambda u$) contains a portion of the imaginary axis. Hence, for sufficiently small time step $\Delta t > 0$, the products of Δt times the eigenvalues of the spatial operator for the Fourier approximations to periodic advection problems lie entirely in the stability region; the AB3 method is stable for this particular problem.

The AB3 method is a three-level scheme. To use this method, we need to provide the values of f at time Δt and $2\Delta t$, in advance. There are many ways to get f^1 and f^2, and using the Euler method is one possibility. In the following, when we mention the AB3 method, that means we use the Euler method first to obtain f^1 and f^2, then we use the AB3 method to get approximations of f^n for $n \geq 3$.

Combining the spectral term discretized in time using the AB3 method, and the difference approximation to f_r (14), our overall method for Eq. (13) is

$$f_{i,j}^{n+1} = f_{i,j}^n - \Delta t r_i p_j \frac{f_{i+1/2,j}^{n+1/2} - f_{i-1/2,j}^{n+1/2}}{\Delta r} - \Delta t q_j \left[D_\theta f^n\right]_{i,j}^{\text{AB3}}. \tag{15}$$

Here, $p_j = p(\theta_j)$, $q_j = q(\theta_j)$, and

$$\left[D_\theta f^n\right]_{i,j}^{\text{AB3}} = \frac{23}{12}\left[D_\theta f^n\right]_{i,j} - \frac{16}{12}\left[D_\theta f^{n-1}\right]_{i,j} - \frac{5}{12}\left[D_\theta f^{n-2}\right]_{i,j}.$$

The computational grid points in the r direction are extended by two cells, so the cell edge values of f on the original boundary can be determined. The normal velocity at each boundary point possibly points inward or outward, or is even still. We therefore set the boundary conditions for the extra two cells in the r direction as follows: If $p(\theta_j) > 0$, that is, the boundary condition is outflow, we use zero order extrapolation from the interior of the domain to obtain

$$f_{M+1,j}^n = f_{M+2,j}^n = f_{M,j}^n.$$

If $p(\theta_j) \leq 0$, i.e., inflow or no-flow boundary condition, we set

$$f_{M+1,j}^n = f_{M+2,j}^n = 0.$$

We also need a value of f at $r = 0$, which we take as the cell average of f over a disc $r \leq \frac{\Delta r}{2}$. For a half disc H_R of radius $R = \frac{\Delta r}{2}$ centered at $r = 0$, we integrate (13) over H_R and assume that R is small and that f is constant in (r, θ) within H_R. We get

$$\frac{d}{dt}f(0, -, t)\frac{\pi R^2}{2} = -R^2 \int_0^\pi p(\theta)f(R, \theta, t)\, d\theta. \tag{16}$$

We use a discrete version of (16), namely

$$f_0^{n+1} = f_0^n - \frac{2\Delta t}{\pi} \sum_{j=1}^{N} p(\theta_j) f\left(\frac{\Delta r}{2}, \theta_j, t^{n+1/2}\right) \frac{\pi}{N}$$

$$= f_0^n - \frac{2\Delta t}{N} \sum_{j=1}^{N} p_j f_{1/2,j}^{n+1/2}. \tag{17}$$

To test our method for Eq. (13) we apply it in the case

$$p(\theta) = \frac{1}{2} \sin 2\theta, \qquad q(\theta) = -\sin^2 \theta,$$

which corresponds to the shear flow $\mathbf{u} = (y - 0.5, 0)$. With this choice of p and q, (13) becomes

$$f_t + \frac{r}{2} \sin 2\theta f_r - \sin^2 \theta f_\theta = 0. \tag{18}$$

We take as initial condition

$$f(r, \theta, 0) = \frac{1}{2}[1 - \tanh \alpha (r - 0.2)], \qquad \alpha = 15, \tag{19}$$

and find (after tedious calculation) that the true solution is

$$f(r, \theta, t) = \frac{1}{2}[1 - \tanh \alpha (r(1 - t \sin 2\theta + t^2 \sin^2 \theta)^{1/2} - 0.2)]. \tag{20}$$

We fix $\Delta r = \frac{1}{64}$, $\Delta t = \frac{5}{64^2}$, and vary $\Delta\theta$ from $\frac{\pi}{16}$ to $\frac{\pi}{64}$. Up to $t = 1000 * \Delta t$, the numerical solution with $\Delta\theta = \frac{\pi}{16}$ is smooth. After that, the shear flow makes the support of f thinner and thinner, and the numerical solution displays nonphysical ripples. Reducing Δr or Δt does not get rid of these errors. The situation improves with smaller $\Delta\theta$. Figure 2 shows that the numerical solution with $\Delta\theta = \frac{\pi}{64}$ is a good approximation even at $t = 2000 * \Delta t$.

If the velocity is multiplied by $\cos(2\pi t)$, that is, we solve

$$f_t + \cos(2\pi t)\left[\frac{r}{2} \sin 2\theta f_r - \sin^2 \theta f_\theta\right] = 0, \tag{21}$$

along with the initial condition (19), then no ripples are seen even if with $\Delta\theta = \frac{\pi}{16}$. Hence, we believe that the occurrence of ripples is due to the rapid transition in f induced by the shear flow, where the solution has a very narrow distribution in θ.

Equations (18) and (19) are used to do the computational analysis of convergence. Table I shows that when Δr and Δt are each halved, the error is reduced by a factor of 4 through time $= 2.441406$ with $\Delta\theta = \frac{\pi}{64}$. After that, the error ratio increases very quickly since $\Delta\theta = \frac{\pi}{64}$ is not small enough to resolve the changes of f and hence some ripples occur. Using $\Delta\theta = \frac{\pi}{32}$, the solution is well approximated through time $= 1.220703$, and Table II shows that the error ratio is about $\frac{1}{4}$ until that time. These data provide evidence that the scheme is second order accurate in both space and time.

The function $f(r, \theta, t)$ in the test problem corresponds to the function $E(\mathbf{x}, \mathbf{v}, t)$ in the full model. Recall that it is not E itself which influences the dynamics in the model system
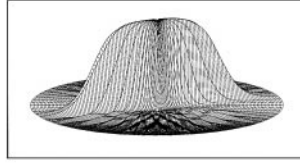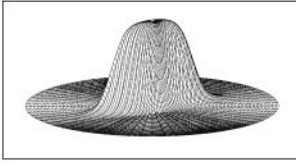
TABLE I

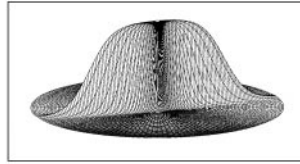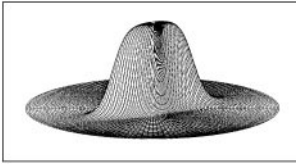**Convergence Analysis of Advective Form with $\Delta\theta = \frac{\pi}{64}$**

| Time	Norm	Case $\Delta r = \frac{1}{32}$ $\Delta t = \frac{10}{64^2}$	$\Delta r = \frac{1}{64}$ $\Delta t = \frac{5}{64^2}$	$\Delta r = \frac{1}{128}$ $\Delta t = \frac{2.5}{64^2}$	$\frac{\text{case 2}}{\text{case 1}}$	$\frac{\text{case 3}}{\text{case 2}}$
0.610352	1-n	8.86×10^{-4}	2.04×10^{-4}	4.81×10^{-5}	0.230	0.236
	2-n	2.54×10^{-3}	5.92×10^{-4}	1.41×10^{-4}	0.233	0.238
1.220703	1-n	1.67×10^{-3}	3.85×10^{-4}	9.02×10^{-5}	0.231	0.234
	2-n	4.50×10^{-3}	1.14×10^{-3}	2.77×10^{-4}	0.253	0.243
1.831055	1-n	2.35×10^{-3}	5.51×10^{-4}	1.30×10^{-4}	0.234	0.236
	2-n	6.15×10^{-3}	1.71×10^{-3}	4.15×10^{-4}	0.278	0.243
2.441406	1-n	3.04×10^{-3}	8.14×10^{-4}	2.66×10^{-4}	0.268	0.327
	2-n	8.10×10^{-3}	2.32×10^{-3}	5.84×10^{-4}	0.286	0.252
3.051758	1-n	4.32×10^{-3}	2.28×10^{-3}	1.74×10^{-3}	0.528	0.763
	2-n	9.03×10^{-3}	3.35×10^{-3}	1.80×10^{-3}	0.371	0.537
3.662109	1-n	6.43×10^{-3}	4.56×10^{-3}	3.97×10^{-3}	0.709	0.871
	2-n	1.13×10^{-2}	6.39×10^{-3}	5.44×10^{-3}	0.565	0.851
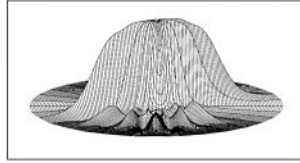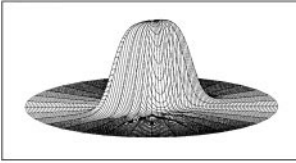
(a) $N = 16$

(b) $N = 32$

(c) $N = 64$
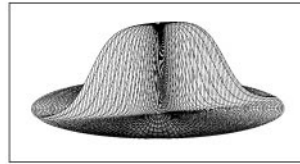
(d) true solution

FIG. 2. Solutions of $f_t + \frac{r}{2}\sin 2\theta f_r - \sin^2\theta f_\theta = 0$ at selected times. Parts (a), (b), and (c) are numerical solutions with $\Delta\theta = \frac{\pi}{N}$, $N = 16, 32, 64$, respectively; (d) is the true solution.

TABLE II
Convergence Analysis of Advective Form with $\Delta\theta = \frac{\pi}{32}$

		Case				
		$\Delta r = \frac{1}{32}$	$\Delta r = \frac{1}{64}$	$\Delta r = \frac{1}{128}$		
Time	Norm	$\Delta t = \frac{10}{64^2}$	$\Delta t = \frac{5}{64^2}$	$\Delta t = \frac{2.5}{64^2}$	$\frac{\text{case 2}}{\text{case 1}}$	$\frac{\text{case 3}}{\text{case 2}}$
0.610352	1-n	8.85×10^{-4}	2.04×10^{-4}	4.81×10^{-5}	0.231	0.236
	2-n	2.54×10^{-3}	5.92×10^{-4}	1.41×10^{-4}	0.233	0.238
1.220703	1-n	1.67×10^{-3}	3.91×10^{-4}	9.75×10^{-5}	0.234	0.249
	2-n	4.50×10^{-3}	1.14×10^{-3}	2.78×10^{-4}	0.253	0.244
1.831055	1-n	2.87×10^{-3}	1.12×10^{-3}	7.95×10^{-4}	0.390	0.710
	2-n	6.20×10^{-3}	1.96×10^{-3}	1.07×10^{-3}	0.316	0.546
2.441406	1-n	1.17×10^{-2}	1.03×10^{-2}	9.96×10^{-3}	0.880	0.967
	2-n	1.43×10^{-2}	1.18×10^{-2}	1.13×10^{-2}	0.825	0.958

but rather the cohesion stress tensor $\underline{\underline{\sigma}}^p(\mathbf{x}, t)$ (or its divergence $\mathbf{f}^p$) and that $\underline{\underline{\sigma}}^p$ is obtained from E by integration over $\mathbf{v}$ (see Eq. (8)).

To get some idea about the sensitivity of $\underline{\underline{\sigma}}^p(\mathbf{x}, t)$ to changes in the numerical parameters, particularly $\Delta\theta$, we considered a modified test problem. This problem differs from that above in that it has terms that mimic those in Eq. (11) that describe elastic link formation and breaking,

$$f_t + rp(\theta)f_r + q(\theta)f_\theta = \alpha(r) - \beta(r)f$$

with $\alpha(r) = 1$ for $r < 0.2$, and $\alpha(r) = 0$ otherwise, and $\beta(r) = 0.1$ for $r < 0.3$, and $\beta(r) = 10.0$ otherwise. By analogy with Eq. (12), we defined the stress tensor $\underline{\underline{\sigma}}^p$ from $f(r, \theta, t)$ by the integral

$$\underline{\underline{\sigma}}^p = \frac{1}{2} \int f(r, \theta, t) S(r) \begin{pmatrix} r\cos\theta \\ r\sin\theta \end{pmatrix} (r\cos\theta, r\sin\theta) r \, dr \, d\theta.$$

We considered how the principal directions and rates of stress (the unit eigenvectors and eigenvalues of $\underline{\underline{\sigma}}^p$) varied with t for different choices of $\Delta\theta$. We found that in all cases the eigenvectors rotated consistent with the shearing flow and that the directions of the eigenvectors and the magnitudes of the eigenvalues were almost the same for values of $\Delta\theta$ from $\frac{\pi}{128}$ to $\frac{\pi}{8}$ even at late times when f itself showed substantial rippling for the larger values of $\Delta\theta$. We interpret this as indicating that the integrated quantities of interest are accurately captured even with relatively crude discretizations in the θ direction.

3. ADVECTION ALGORITHM

Several equations in the aggregation models include advection of a quantity in a two-dimensional incompressible velocity field. The method we use to discretize the advective terms in Eqs. (3)–(6) is LeVeque's high-resolution advection algorithm [20] as implemented in his CLAWPACK software package [19]. Here we briefly describe LeVeque's algorithm.

LeVeque's algorithm is concerned with solution of a scalar advection equation of the form

$$f_t + \mathbf{u} \cdot \nabla f = 0, \tag{22}$$

where the velocity field $\mathbf{u}(\mathbf{x}, t)$ is incompressible. The method does *not* rely on operator splitting to sequentially treat the x-derivatives and then the y-derivatives. This is important in order to avoid artificial compressibility effects. Because of the incompressibility condition $\nabla \cdot \mathbf{u} = 0$, the *advective* form Eq. (22) can also be written in *conservative* form as

$$f_t + \nabla \cdot (\mathbf{u} f) = 0.$$

These are equivalent for the differential equations, but discretizations based on the advective form are generally different from and often superior to those based on the conservative form. Among the advantages of advective differencing is better treatment of patches of constant f. On the other hand, advective differences may not preserve total mass. LeVeque's algorithm proceeds in several steps, the first corresponding to a first-order upwind method, and the later steps giving a series of improvements to this basic method. The algorithm is a hybrid in that the first step is written in advective form while the correction terms, though based on advective differences, are written in terms of flux differences. The resulting algorithm has the good features of an advective differencing, but is fully conservative provided the discrete incompressibility condition given below holds. The method interprets f_{ij}^n as the cell-average of f at time $t^n = nk$ over the cell $C_{i,j} \equiv [x_i - h/2, x_i + h/2] \times [y_j - h/2, y_j + h/2]$ shown in Fig. 3. It makes use of the cell-edge velocities shown in that figure. The notations $F_{i+1/2,j}$ and $G_{i,j+1/2}$ are used to denote numerical fluxes across the right and top edges, respectively, of cell $C_{i,j}$.

We first describe the steps involved in updating $\{f_{ij}^n\}$ to $\{f_{ij}^{n+1}\}$ and then we interpret them. For simplicity, we describe the algorithm as if the velocities u and v were everywhere positive. The actual algorithm can, of course, handle velocities of varying signs. The difference between what we describe and the true algorithm is some additional logic to determine and use data from the upwind direction for each cell edge.
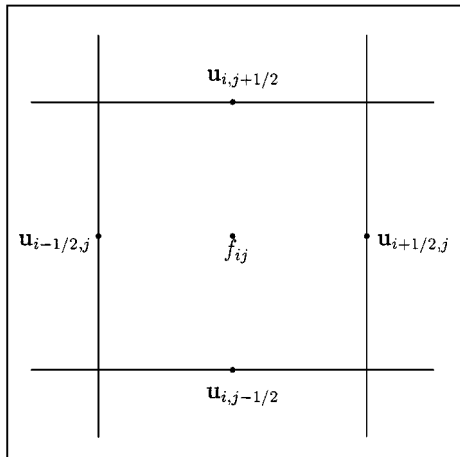

FIG. 3.   Advection grid and interface velocities.

The first step of the method can be written in advective form as

$$f_{ij}^* = f_{ij}^n - \frac{k}{h}\{u_{i-1/2,j}^{n+1/2}(f_{ij}^n - f_{i-1,j}^n) + v_{i,j-1/2}^{n+1/2}(f_{ij}^n - f_{i,j-1}^n)\}. \tag{23}$$

Here, the notation f_{ij}^* is used to indicate an intermediate value of f, not the final value at the end of the time step. Because of its advective form, this differencing clearly preserves constant f exactly. It turns out that, provided the discrete incompressibility condition

$$u_{i+1/2,j}^{n+1/2} - u_{i-1/2,j}^{n+1/2} + v_{i,j+1/2}^{n+1/2} - v_{i,j-1/2}^{n+1/2} = 0 \tag{24}$$

holds, the advective differencing is exactly equivalent to the conservative differencing defined by

$$F_{i-1/2,j} = u_{i-1/2,j}^{n+1/2} f_{i-1,j}^n \tag{25}$$

$$G_{i,j-1/2} = v_{i,j-1/2}^{n+1/2} f_{i,j-1}^n \tag{26}$$

$$f_{ij}^* = f_{ij}^n - \frac{k}{h}\{F_{i+1/2,j} - F_{i-1/2,j} + G_{i,j+1/2} - G_{i,j-1/2}\}. \tag{27}$$

So Step 1 can be thought of in either form. For the following description as well as the implementation in CLAWPACK, it is most convenient to think of the cell-edge fluxes as being initialized to zero, and then Step 1 consists of updating the fluxes by:

Step 1.

$$F_{i-1/2,j} := F_{i-1/2,j} + u_{i-1/2,j}^{n+1/2} f_{i-1,j}^n \tag{28}$$

$$G_{i,j-1/2} := G_{i,j-1/2} + v_{i,j-1/2}^{n+1/2} f_{i,j-1}^n. \tag{29}$$

During Steps 2, 3, and 4, the cell-edge fluxes are further modified as follows:

Step 2.

$$G_{i,j+1/2} := G_{i,j+1/2} - \frac{1}{2}\frac{k}{h}u_{i-1/2,j}^{n+1/2}v_{i-1/2,j}^{n+1/2}(f_{ij}^n - f_{i-1,j}^n) \tag{30}$$

$$F_{i+1/2,j} := F_{i+1/2,j} - \frac{1}{2}\frac{k}{h}u_{i,j-1/2}^{n+1/2}v_{i,j-1/2}^{n+1/2}(f_{ij}^n - f_{i,j-1}^n). \tag{31}$$

Step 3.

$$F_{i-1/2,j} := F_{i-1/2,j} + \frac{1}{2}|u_{i-1/2,j}^{n+1/2}|\left(1 - \frac{k}{h}|u_{i-1/2,j}^{n+1/2}|\right)(f_{ij}^n - f_{i-1,j}^n)\Phi_{i-1/2,j} \tag{32}$$

$$G_{i,j-1/2} := G_{i,j-1/2} + \frac{1}{2}|v_{i,j-1/2}^{n+1/2}|\left(1 - \frac{k}{h}|v_{i,j-1/2}^{n+1/2}|\right)(f_{ij}^n - f_{i,j-1}^n)\Phi_{i,j-1/2}, \tag{33}$$

where $\Phi_{i-1/2,j}$ and $\Phi_{i,j-1/2}$ are flux limiters which depend on local values of $\{f_{ij}^n\}$ along the lines $y = y_j$ and $x = x_i$, respectively.

Step 4.

$$G_{i-1,j+1/2} := G_{i-1,j+1/2} - \frac{k}{h} v_{i-1/2,j}^{n+1/2} \frac{1}{2} \left| u_{i-1/2,j}^{n+1/2} \right|$$

$$\times \left(1 - \frac{k}{h} \left| u_{i-1/2,j}^{n+1/2} \right| \right) \left(f_{ij}^n - f_{i-1,j}^n \right) \Phi_{i-1/2,j} \tag{34}$$

$$G_{i,j+1/2} := G_{i,j+1/2} + \frac{k}{h} v_{i-1/2,j}^{n+1/2} \frac{1}{2} \left| u_{i-1/2,j}^{n+1/2} \right|$$

$$\times \left(1 - \frac{k}{h} \left| u_{i-1/2,j}^{n+1/2} \right| \right) \left(f_{ij}^n - f_{i-1,j}^n \right) \Phi_{i-1/2,j} \tag{35}$$

$$F_{i+1/2,j-1} := F_{i+1/2,j-1} - \frac{k}{h} u_{i,j-1/2}^{n+1/2} \frac{1}{2} \left| v_{i,j-1/2}^{n+1/2} \right|$$

$$\times \left(1 - \frac{k}{h} \left| v_{i,j-1/2}^{n+1/2} \right| \right) \left(f_{ij}^n - f_{i,j-1}^n \right) \Phi_{i,j-1/2} \tag{36}$$

$$F_{i+1/2,j} := F_{i+1/2,j} + \frac{k}{h} u_{i,j-1/2}^{n+1/2} \frac{1}{2} \left| v_{i,j-1/2}^{n+1/2} \right|$$

$$\times \left(1 - \frac{k}{h} \left| v_{i,j-1/2}^{n+1/2} \right| \right) \left(f_{ij}^n - f_{i,j-1}^n \right) \Phi_{i,j-1/2}. \tag{37}$$

The final values $\{f_{ij}^{n+1}\}$ are then obtained from

$$f_{ij}^{n+1} = f_{ij}^n - \frac{k}{h} \{ F_{i+1/2,j} - F_{i-1/2,j} + G_{i,j+1/2} - G_{i,j-1/2} \}. \tag{38}$$

LeVeque's advection algorithm was derived using a *wave propagation* perspective also used successfully for multidimensional nonlinear conservation laws [17, 18]. The interpretation of the steps of the algorithm is made with reference to Fig. 4 as follows: For Step 1, we imagine that a piecewise constant function is constructed with value f_{ij}^n in all of cell $C_{i,j}$. Then Eq. (28) accounts for the normal propagation of the value $f_{i-1,j}^n$ from cell $C_{i-1,j}$ to cell $C_{i,j}$, while Eq. (29) accounts for the normal propagation of the value $f_{i,j-1}^n$ from cell $C_{i,j-1}$ to cell $C_{i,j}$. (Recall that in this discussion we assume that u and v are everywhere positive.) These fluxes are shown in Fig. 4a. If these were taken as the final values of the fluxes, the resulting method would be a simple first order upwind procedure. Step 2 also takes into account transverse propagation of the piecewise constant function. The upward motion of the wave which crosses the cell edge between cells $C_{i-1,j}$ and $C_{i,j}$ affects the cell averages in cells $C_{i,j}$ and $C_{i,j+1}$ and this can be accounted for by the modification to the flux $G_{i,j+1/2}$ given in Eq. (30). The modification is proportional to the area of the shaded triangle in Fig. 4b which is $\frac{1}{2} k^2 u_{i-1/2,j}^{n+1/2} v_{i-1/2,j}^{n+1/2}$. Similarly, the rightward motion of the wave which crosses the cell edge between cells $C_{i,j-1}$ and $C_{i,j}$ affects the cell averages in cells $C_{i,j}$ and $C_{i+1,j}$. This is accounted for by modifying the flux $F_{i+1/2,j}$ as done in Eq. (31). If the fluxes after Step 2 were used to update $\{f_{ij}\}$, the method would still be first order but would have a smaller error constant and better stability properties than the simple upwind method. For Step 3, linear approximations are used to represent the solution in each cell in order to obtain a second-order method. Since the propagation of the cell averages have already been accounted for in Steps 1 and 2, these linear approximations have mean 0. For the propagation in the x-direction, the approximation in cell $C_{i,j}$ is linear in x with slope $\frac{1}{h}(f_{ij}^n - f_{i-1,j}^n)\Phi_{i-1/2,j}$ and is constant in y. The limiter $\Phi_{i-1/2,j}$ is used to prevent the introduction of spurious oscillations or overshoots near steep gradients in f.
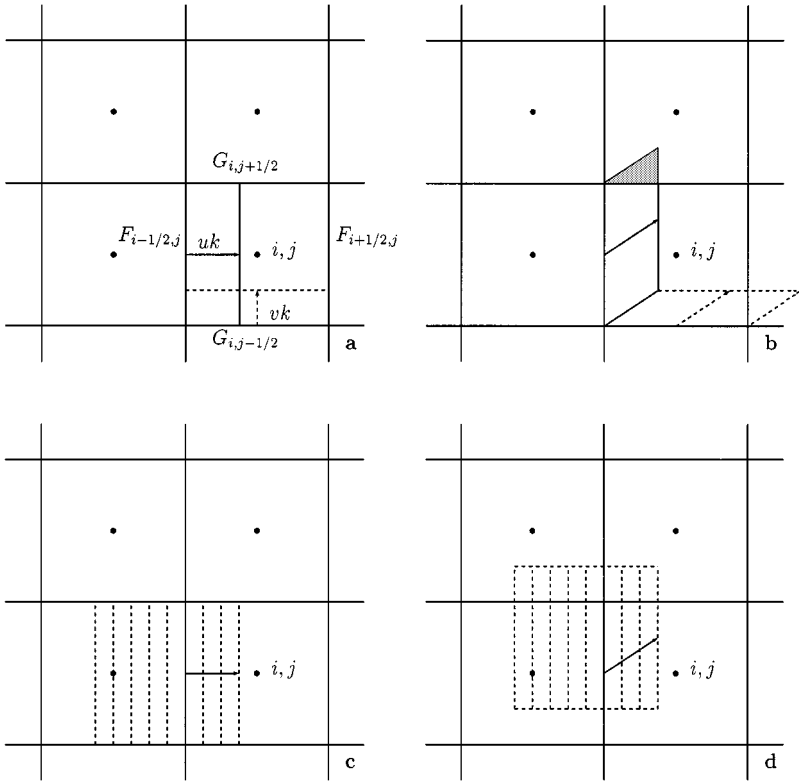
FIG. 4. Geometric picture of LeVeque's advection algorithm. (a) Normal propagation of piecewise constant cell values at speeds $u = u_{i-1/2,j}^{n+1/2}$ and $v = v_{i,j-1/2}^{n+1/2}$. (b) Transverse propagation of piecewise constant cell values. Area of shaded triangle is $\frac{1}{2}k^2 u_{i-1/2,j}^{n+1/2} v_{i-1/2,j}^{n+1/2}$. (c) Normal propagation of correction wave at speed $u_{i-1/2,j}^{n+1/2}$. Dashed lines are contours of the linear approximation in cell $C_{i-1,j}$. (d) Transverse propagation of the correction wave with velocity $(u_{i-1/2,j}^{n+1/2}, v_{i-1/2,j}^{n+1/2})$.

Normal propagation of this linear function from cell $C_{i-1,j}$ into cell $C_{i,j}$ corresponds to the modification to flux $F_{i-1/2,j}$ given in Eq. (32) and to the picture in Fig. 4c. Similarly, an approximation to f which in each cell is linear in y and constant in x gives rise to the modification to flux $G_{i,j-1/2}$ given in Eq. (33). If the fluxes after this step were used to update $\{f_{ij}\}$, the method would be second-order accurate. Even without the limiters, it would differ from the Lax–Wendroff scheme because of its use of upwind differencing. LeVeque calls the waves which correspond to Step 3 *correction* waves. Step 4 accounts for the transverse propagation of the correction waves. The upward motion of the correction wave between cells $C_{i-1,j}$ and $C_{i,j}$ affects the fluxes across the top edges of both of these cells. (See Fig. 4d.) This is accounted for in Eqs. (34)–(35). Note that these changes are just $\pm \frac{k}{h} v_{i-1/2,j}^{n+1/2}$ times the changes in Eq. (32) and so are easy to calculate. In a similar way, the rightward motion of the correction wave between cells $C_{i,j-1}$ and $C_{i,j}$ affects the two fluxes modified in Eqs. (36)–(37). The transverse propagation of the correction waves does not change the formal order of accuracy of the method, but, in LeVeque's computational experiments, it often substantially reduced the magnitude of the error.

LeVeque's algorithm requires that the discrete incompressibility condition (24) be satisfied at time $(n + 1/2)k$. Chorin's scheme, which we use to solve the Navier–Stokes

equations, enforces a different discrete incompressibility condition, $u^n_{i+1,j} - u^n_{i-1,j} + v^n_{i,j+1} - v^n_{i,j-1} = 0$, at each time level n. We define cell-edge velocities from the grid velocities determined by Chorin's scheme as

$$\mathbf{u}^{n+1/2}_{i-1/2,j} = \frac{1}{4}\{\mathbf{u}^n_{i,j} + \mathbf{u}^{n+1}_{i,j} + \mathbf{u}^n_{i-1,j} + \mathbf{u}^{n+1}_{i-1,j}\}$$

$$\mathbf{u}^{n+1/2}_{i,j-1/2} = \frac{1}{4}\{\mathbf{u}^n_{i,j} + \mathbf{u}^{n+1}_{i,j} + \mathbf{u}^n_{i,j-1} + \mathbf{u}^{n+1}_{i,j-1}\}. \tag{39}$$

It is easy to check that these satisfy (24).

4. NUMERICAL METHOD FOR THE E EQUATION

For the elastic link transport equation (11) (the "E equation"), we use LeVeque's high-resolution method (discussed in Section 3) for the advection terms in the **x**-plane, the Fourier-collocation spectral method (discussed in Section 2) for the θ-derivative, and the finite-difference method based on the Bell and Marcus approach for the r-derivative. Then the cohesion force density $\mathbf{f}^p$ due to link formations is approximated by numerical quadrature of Eq. (12).

To test this method, we consider a special model, for which the analytical solution can be derived and compared with the numerical solution. The right hand side of Eq. (11) is set to be zero and the velocity field is the shear flow, $\mathbf{u} = u_0(y - 0.5, 0)$ with u_0 constant. Then the equation of interest is

$$E_t + u_0\left(y - \frac{1}{2}\right)E_x + r\frac{u_0 \sin 2\theta}{2}E_r - u_0 \sin^2 \theta E_\theta = 0. \tag{40}$$

For a similar equation but without x-dependence,

$$g_t + r\frac{u_0 \sin 2\theta}{2}g_r - u_0 \sin^2 \theta g_\theta = 0,$$

and with initial condition

$$g(r, \theta, 0) = \frac{1}{2}[1 - \tanh \alpha_1(r - 0.2)], \qquad \alpha_1 = \text{constant}, \tag{41}$$

the exact solution is

$$g(r, \theta, t) = \frac{1}{2}\{1 - \tanh \alpha_1[r(1 - u_0 t \sin 2\theta + (u_0 t)^2 \sin^2 \theta)^{1/2} - 0.2]\}. \tag{42}$$

Also for the equation

$$\psi_t + u_0\left(y - \frac{1}{2}\right)\psi_x = 0,$$

with initial data

$$\psi(x, y, 0) = \frac{1}{2}\left\{1 - \tanh\alpha_2\left[\left(x - \frac{1}{2}\right)^2 + \left(y - \frac{1}{2}\right)^2 - \left(\frac{3}{16}\right)^2\right]\right\}, \qquad \alpha_2 = \text{constant},$$

(43)

the analytic solution is

$$\psi(x, y, t) = \frac{1}{2}\left\{1 - \tanh\alpha_2\left[\left(x - u_o t\left(y - \frac{1}{2}\right) - \frac{1}{2}\right)^2 + \left(y - \frac{1}{2}\right)^2 - \left(\frac{3}{16}\right)^2\right]\right\}.$$ (44)

It follows that the exact solution to (40) with initial condition $g(r, \theta, 0) \times \psi(x, y, 0)$ is

$$E(\mathbf{x}, \mathbf{v}, t) = E(x, y, r, \theta, t) = g(r, \theta, t)\psi(x, y, t). \qquad (45)$$

Hence the gradient of E in the $\mathbf{x}$-plane is

$$\nabla_\mathbf{x} E(\mathbf{x}, r, \theta, t) = g(r, \theta, t)\nabla_\mathbf{x}\psi(\mathbf{x}, t) = g(r, \theta, t)\begin{pmatrix} a(\mathbf{x}, t) \\ b(\mathbf{x}, t) \end{pmatrix}, \qquad (46)$$

where $a(\mathbf{x}, t) = \frac{\partial\psi}{\partial x}(\mathbf{x}, t)$ and $b(\mathbf{x}, t) = \frac{\partial\psi}{\partial y}(\mathbf{x}, t)$. The cohesion force can be calculated as

$$\begin{aligned}
\mathbf{f}^p(\mathbf{x}, t) &= \frac{1}{2}\int(\mathbf{v} \cdot \nabla_\mathbf{x} E)S(|\mathbf{v}|)\mathbf{v}\,d\mathbf{v} \\
&= \frac{1}{2}\int g(\mathbf{v}, t)\begin{pmatrix} v_1^2 a(\mathbf{x}, t) + v_1 v_2 b(\mathbf{x}, t) \\ v_1 v_2 a(\mathbf{x}, t) + v_2^2 b(\mathbf{x}, t) \end{pmatrix}S(|\mathbf{v}|)\,d\mathbf{v} \\
&= \begin{pmatrix} a(\mathbf{x}, t)I_1 + b(\mathbf{x}, t)I_2 \\ a(\mathbf{x}, t)I_2 + b(\mathbf{x}, t)I_3 \end{pmatrix},
\end{aligned}$$

(47)

where

$$I_1 = \frac{1}{2}\int g(\mathbf{v}, t)v_1^2 S(|\mathbf{v}|)\,d\mathbf{v} = \int_0^{\bar{r}}\int_0^\pi \cos^2\theta g(r, \theta, t)S(r)r^3 d\theta\,dr,$$

$$I_2 = \frac{1}{2}\int g(\mathbf{v}, t)v_1 v_2 S(|\mathbf{v}|)\,d\mathbf{v} = \int_0^{\bar{r}}\int_0^\pi \sin\theta\cos\theta g(r, \theta, t)S(r)r^3 d\theta\,dr,$$

$$I_3 = \frac{1}{2}\int g(\mathbf{v}, t)v_2^2 S(|\mathbf{v}|)\,d\mathbf{v} = \int_0^{\bar{r}}\int_0^\pi \sin^2\theta g(r, \theta, t)S(r)r^3 d\theta\,dr.$$

So, we can calculate E exactly from (45), $\nabla_\mathbf{x} E$ exactly from (46), and $\mathbf{f}^p$ from (47) with numerical quadrature used to evaluate the integrals I_1, I_2, and I_3. We can compare the results with those obtained by solving (40) numerically to obtain $\tilde{E}$, followed by use of a central difference formula to approximate $\nabla_\mathbf{x} E$ and numerical integration to find $\tilde{\mathbf{f}}^p(\mathbf{x}, t)$.

Table III shows the comparison between the true solution and the approximated solution at time $= 0.2441406$, with $\alpha_1 = 15$, $\alpha_2 = 25$, and $\Delta\theta = \frac{\pi}{16}$. When Δr is fixed, and the mesh size in $\mathbf{x}$-space is decreased, the error in E, $\|E - \tilde{E}\|$, changes little, but the errors in the partial derivatives $\|E_x - \tilde{E}_x\|$ and $\|E_y - \tilde{E}_y\|$ decrease by a factor of about 3; when $\Delta x = \Delta y$ are fixed, and Δr is decreased, $\|E - \tilde{E}\|$ decreases by a factor of about 3, whereas

TABLE III
Comparison between E and $\tilde{E}$ at Time = 0.2441406

	$\Delta r = \frac{1}{16}, \Delta t = \frac{10}{64^2}$		$\Delta r = \frac{1}{32}, \Delta t = \frac{5}{64^2}$	
	$\Delta x = \Delta y = \frac{1}{16}$	$\Delta x = \Delta y = \frac{1}{32}$	$\Delta x = \Delta y = \frac{1}{32}$	$\Delta x = \Delta y = \frac{1}{64}$
$\lVert E - \tilde{E} \rVert_2$	1.3342×10^{-3}	1.0496×10^{-3}	4.2851×10^{-4}	3.1006×10^{-4}
$\lVert E - \tilde{E} \rVert_1$	2.6345×10^{-4}	1.9225×10^{-4}	7.9515×10^{-5}	5.3449×10^{-5}
$\lVert E_x - \tilde{E}_x \rVert_2$	3.6433×10^{-2}	1.2457×10^{-2}	1.1300×10^{-2}	4.6758×10^{-3}
$\lVert E_x - \tilde{E}_x \rVert_1$	6.1868×10^{-3}	2.2788×10^{-3}	1.8949×10^{-3}	7.8651×10^{-4}
$\lVert E_y - \tilde{E}_y \rVert_2$	3.6600×10^{-2}	1.1879×10^{-2}	1.0577×10^{-2}	3.4377×10^{-3}
$\lVert E_y - \tilde{E}_y \rVert_1$	6.0908×10^{-3}	2.1178×10^{-3}	1.7184×10^{-3}	6.0374×10^{-4}
$\lVert \mathbf{f}^p - \tilde{\mathbf{f}}^p \rVert_2$	2.0506×10^{-4}	7.8375×10^{-5}	6.7151×10^{-5}	2.4220×10^{-5}

the partial derivatives are almost the same. If all of Δx, Δy, and Δr are halved, $\lVert E - \tilde{E} \rVert$, $\lVert E_x - \tilde{E}_x \rVert$, $\lVert E_y - \tilde{E}_y \rVert$, and $\lVert \mathbf{f}^p - \tilde{\mathbf{f}}^p \rVert$ are reduced by a factor of 3.3. So, the numerical method displayed between first and second order convergence on this problem. Figure 5 displays the force field for $\mathbf{f}^p$ and $\tilde{\mathbf{f}}^p$ with $\Delta x = \Delta y = \Delta r = \frac{1}{32}$. Little difference between them is evident.
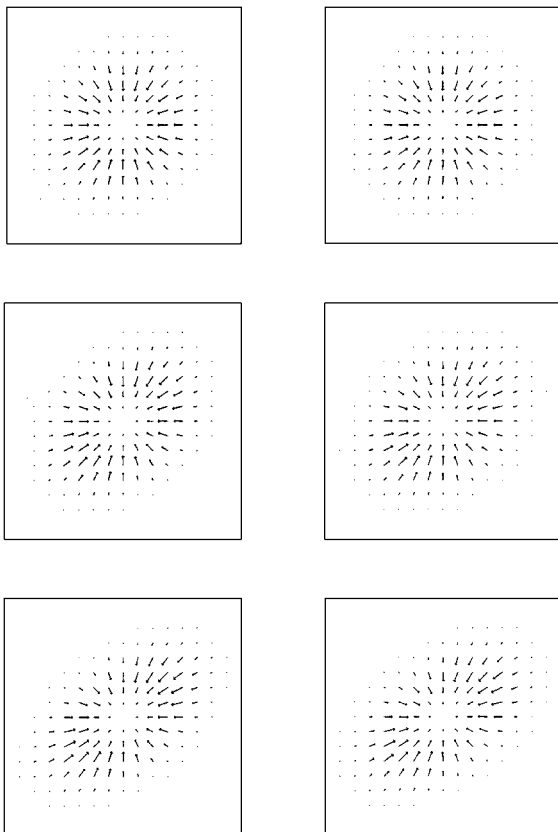
FIG. 5. Force fields on shear flow at sequential times. Left column represents the results from the true solution E; right column results are obtained from the numerical solution $\tilde{E}$.

5. NUMERICAL EXPERIMENTS ON FULL MODELS

5.1. *Algorithms for Full Models*

To simulate the general form of the aggregation continuum models based on Eqs. (1)–(7), we discretize them spatially and temporally. We assume that the fluid domain is square and that the spatial step sizes in the x and y directions are equal. The boundary condition of the domain is periodic which indicates that corresponding discretized points on the left and right, and on the top and bottom boundaries are identical.

We use Chorin's projection-based finite difference method [8] to solve the Navier–Stokes equations (1)–(2). For the transport of the nonactivated platelet density and ADP concentration in Eqs. (3) and (5), we couple LeVeque's high-resolution conservative algorithm for advection in incompressible flow [20] for the advection terms with an alternating-directional-implicit (ADI) method [21] for the diffusive terms. This is done by Strang-splitting to more accurately calculate their transport. We also combine LeVeque's high-resolution method for the advection term with a hybrid finite difference-spectral method for the (r, θ) terms to solve for the interplatelet link density in Eq. (6) (demonstrated in Section 4). The nonlinear reaction terms of Eqs. (3)–(6) are calculated using analytical solutions which are based on the fact that $R(c)$ is assumed to be a step function. Finally, the cohesion force density is approximated by numerical quadrature.

Having described the individual numerical methods for each term in the continuum models, we summarize the complete numerical procedure for advancing the full models a single time step:

(1) Use the current values of the interplatelet link density E to obtain the cohesion force density $\mathbf{f}^p$ via Eq. (7).

(2) Solve the Navier–Stokes equations (1)–(2) with the new force $\mathbf{f}^p$ to determine the velocity field $\mathbf{u}$. At the end of this step, both $\mathbf{u}^n$ and $\mathbf{u}^{n+1}$ are available. These are used to define the half-time level velocity $\mathbf{u}^{n+1/2}$ needed in the advective algorithm.

(3) Update the densities of ϕ_n, ϕ_a, c, and E in Eqs. (3)–(6) to account for the advective and diffusive transports.

(4) Update further the variables ϕ_n, ϕ_a, c, and E to account for their reaction terms.

For visualization purposes, we define a function $z(\mathbf{x}, t)$ as

$$z(\mathbf{x}, t) = \int E(\mathbf{x}, \mathbf{v}, t) \, d\mathbf{v},$$

so that z measures the concentration of links at $\mathbf{x}$ in all directions $\mathbf{v}$. Since aggregation in the models is maintained through the interplatelet links, it is reasonable to call z the aggregation intensity. We can derive a transport equation for z from Eqs. (4) and (6) (see [11])

$$\frac{\partial z}{\partial t} + \mathbf{u} \cdot \nabla z = \phi_a^2 \int \alpha(|\mathbf{v}|) \, d\mathbf{v} - \int \beta(|\mathbf{v}|) E \, d\mathbf{v}.$$

5.2. *Competition with the Link Formation and Breaking*

Whether an aggregate grows or shrinks is influenced by competition between new chemically induced activation and link formation on the one hand, and shear-induced link breaking on the other hand, and we are interested in conducting experiments to study the dynamics of this competition. Real aggregation happens inside blood vessels and involves important

interactions between platelets and the vessel walls. In addition, as a real aggregate grows and projects into the vessel lumen, the space available for flow decreases and consequently the blood flow can be accelerated, perhaps substantially, in the vicinity of the aggregate. This can have several important consequences: The shear stress exerted on the aggregate may increase substantially, and this might limit further aggregate growth because the stresses may become greater than new interplatelet bonds can withstand. If the stresses on an aggregate become large enough, portions of the aggregate may break free from the wall. This is known as embolization and is important medically, because the embolus (the part of the aggregate separated from the wall) can occlude a smaller vessel downstream. The accelerated flow near the wall-bound aggregate may also increase the rate at which activating chemical (ADP) released near the aggregate is washed away, and, while it may increase transport of new nonactivated platelets from upstream into the vicinity of the aggregate, it also reduces the time period during which these platelets are near the aggregate and can become activated and form cohesive bonds with platelets of the aggregate. We would like to simulate and study these processes in a model that includes platelet-wall interactions and the growth of wall-bound platelet aggregates, and we are working to extend our models and numerical methods to handle such situations. For the version of the model addressed in the current paper, which does not allow for platelet adhesion to vessel walls, we modify the set-up used for computational experiments in [11, 12] to directly increase the stresses to which the aggregate is subject, and, in some experiments, to also reduce the recruitment of new platelets to the aggregate.

For these experiments, the background flow was taken to be a spatially periodic stagnation point flow; initially, nonactivated platelets had a uniform distribution ($\phi_n = 1$) and no activated platelets were present ($\phi_a = 0$ and hence $E = 0$); and the initial ADP concentration was taken to have circular support centered on the stagnation point. These assumptions correspond to an experiment in which activating chemical is dropped into a stirred suspension of nonactivated platelets. The pull of the stagnation point flow, along with the release of more ADP and the consequent activation of additional platelets, contributed to the growth of a progressively larger elliptical aggregate. We allowed these factors to increase the area of aggregation for a while, then, to mimic the extra stresses that would be applied to a wall-bound aggregate as the vessel lumen decreased, we applied extra forces to pull outward on the aggregate. We computed the effect of these extra forces for a specific choice of link formation rate and for each of several choices of link breaking rate. Link formation between two activated platelets was assumed to occur only when the distance separating the platelets was about 1. That is, the link formation rate was chosen to be like a bell-shape function centered near $|\mathbf{v}| = 1$ (See curve α in Fig. 6.) Four cases were tested:

1. We assumed that the breaking rate was almost 0 for $|\mathbf{v}| < 1$, increased smoothly between $|\mathbf{v}| = 1$ and $|\mathbf{v}| = 2$ to a constant value for $|\mathbf{v}| > 2$. That is, we assumed that existing links would be broken only very slowly when the linked platelets were very close to one other, and that the links would break at a constant rate when stretched to a length greater than twice a platelet's diameter. This breaking rate function is shown in Fig. 6 (curve β_1).

2. The link breaking rate was similar to that in Case 1 for $|\mathbf{v}| < 1.5$, but increased rapidly (exponentially in $|\mathbf{v}|$) for $|\mathbf{v}| > 1.5$ (curve β_2 in Fig. 6).

3. The breaking rate was the same as in Case 1. In addition, when we imposed the extra forces to pull outward on the aggregate, we simultaneously turned off all new chemically induced platelet activation.
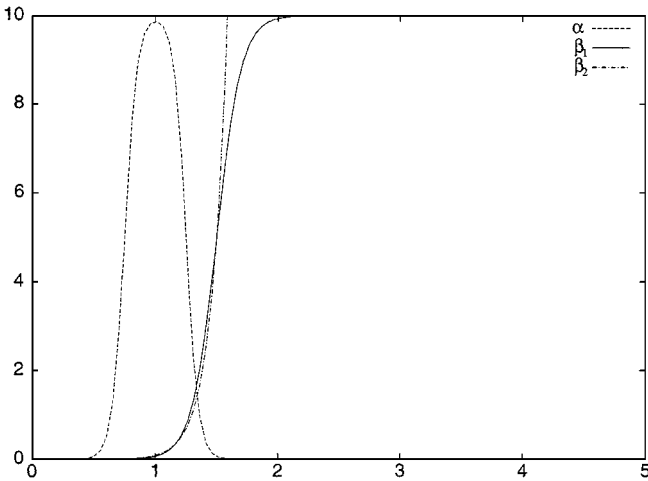
FIG. 6. Creating and breaking link rates. Curve α is a formation link rate; curves β_1 and β_2 are breaking link rates. Horizontal axis is $|\mathbf{v}|$.

4. The exponential link breaking rate function of Case 2 was used, and no further platelet activation was allowed after the extra forces were imposed as in Case 3.

The cessation of platelet activation in Cases 3 and 4 was intended to mimic the effect of faster wash-out of ADP, and the shorter time for activation and aggregation that would accompany increased flow rates over real wall-bound aggregates.

At each of several times, we plotted the velocity field, the activation threshold concentration curve (dashed line), and several contours of the aggregation intensity (solid lines). From the contours and velocity field plots for Cases 1 and 2 in Figs. 7a and 7b, we see only one interior contour of aggregation intensity z breaking for Case 1, and while more z contours break in Case 2, the total aggregate is still intact and the location of the ADP threshold curve in the vicinity of the stagnation point does not change much as time progresses. In Case 1, the link breaking rate β was almost constant when the bonds were long (i.e., $|\mathbf{v}| > 2$), so there is virtually no difference in the rate at which bonds of length, say, $|\mathbf{v}| = 2$ and $|\mathbf{v}| = 3$ break, but each of the latter bonds exerts 50% more force because it is strained 50% more. We think that a population of relatively few long bonds provides much of the force holding the aggregate together in Case 1.

In Case 2, the bond breaking rate increased sharply with $|\mathbf{v}|$ for $|\mathbf{v}| > 2$, but the aggregate still held together. Recall that in Cases 1 and 2 new activation is allowed to continue throughout the experiment. Examination of the flow fields in Fig. 7 shows that nonactivated platelets are carried across the activation-threshold curve (dashed curve) toward the center of the aggregate. These newly activated platelets formed new bonds (with $|\mathbf{v}| \approx 1$ at the time of formation) to strengthen the aggregate. In Case 2 the competition between new activation and formation of short bonds and rapid breaking of long bonds leads to cohesion forces weaker than those in Case 1 but still strong enough to keep the aggregate intact. The formation of new short bonds also contributed to keep the aggregate intact in Case 1.

The influence of new bond formation involving newly activated platelets was eliminated in Cases 3 and 4. In Case 4, long-links also broke quickly, and in Fig. 8b we see that without the compensation of new short bonds, the cohesion force decreased, and the central portion of the aggregate became progressively thinner until the aggregate broke in two!
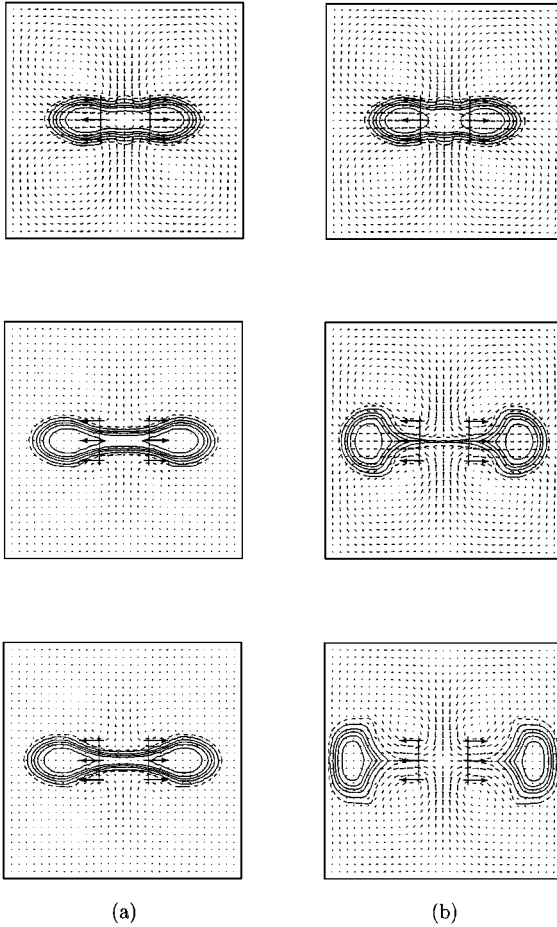
(a)   (b)
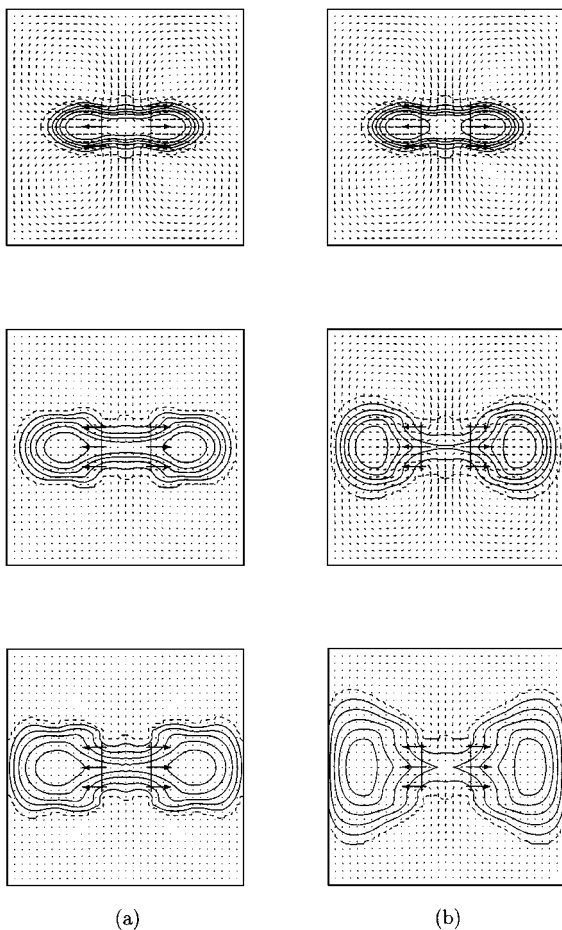
FIG. 7. The effects of link formation and breaking with new activation. (a) Case 1, (b) Case 2. Large arrows and vertical lines indicate locations of imposed extra forces.

This calculation illustrates that, under conditions intended to simulate those which obtain when a wall-bound aggregate grows to block a substantial portion of a vessel, the model aggregates can break up as real aggregates sometimes do. In Case 3 (Fig. 8a), there was less activation than in the corresponding Case 1, but the aggregate held together even when the calculation was carried out to a time 33% later than the breaking time in Case 4. The fact that the aggregate broke in Case 4 but not in Case 3 lends support to our contention that a population of long links helped hold the aggregate together in Case 1 earlier.

5.3. *Mechanical Properties of Platelet Aggregation Systems*

Using the numerical methods we developed for the platelet aggregation continuum models, we also began a preliminary analysis of the *mechanical* or visco-elastic-plastic characteristics of the platelet aggregate composite material. From the full continuum models, the platelet aggregate composite material is affected by platelet activation, link formation and breaking, and fluid motion as time advances. To analyze the mechanical characteristics of this material, we designed a numerical experiment to concentrate only on the composite material itself. The point of these experiments is to see how the bulk mechanical properties

FIG. 8. The effects of link formation and breaking without new activation. (a) Case 3, (b) Case 4. Large arrows and vertical lines indicate locations of imposed extra forces.

of the composite material depend on the link formation and breaking rates, $\alpha(|\mathbf{v}|)$ and $\beta(|\mathbf{v}|)$, on the density of activated platelets, and on the mechanical stiffness, $K(|\mathbf{v}|)$, of individual links.

Our experimental "device" is showed in Fig. 9. Two parallel plates are placed a distance L apart; the bottom one is fixed and the top one is movable. Activated platelets with a uniform concentration $\phi_a = \phi_0$ fill the space between the two plates. When the top plate is dragged to the right at speed v, a uniform shear flow gradually develops in the material.

We solve the system of equations,

$$\rho(\mathbf{u}_t + \mathbf{u} \cdot \nabla \mathbf{u}) = -\nabla p + \mu \Delta \mathbf{u} + \mathbf{f}^{ib} + \mathbf{f}^p, \tag{48}$$

$$\nabla \cdot \mathbf{u} = 0, \tag{49}$$

$$\frac{\partial \phi_a}{\partial t} + \mathbf{u} \cdot \nabla \phi_a = 0, \tag{50}$$

$$E_t + \mathbf{u} \cdot \nabla_{\mathbf{x}} E + (\mathbf{v} \cdot \nabla \mathbf{u}) \cdot \nabla_{\mathbf{v}} E = 0, \tag{51}$$

$$\mathbf{f}^p(\mathbf{x}, t) = \frac{1}{2} \int \mathbf{v} \cdot \nabla_{\mathbf{x}} E(\mathbf{x}, \mathbf{v}, t) S(|\mathbf{v}|) \mathbf{v} \, d\mathbf{v}. \tag{52}$$
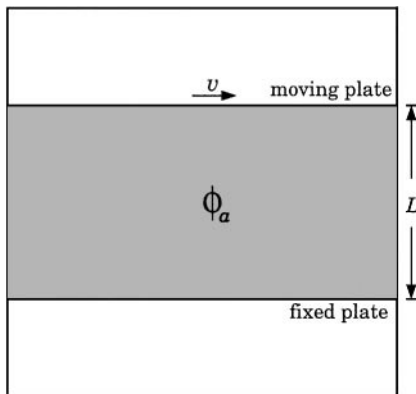
FIG. 9. The device for testing the mechanical properties of platelet aggregate material.

To model the plates, we use the immersed boundary method [23]. Each plate is represented by two strings of immersed boundary points and a set of elastic springs joining the points. There is a spring between each consecutive pair of points in a string, another spring between corresponding points on the two strings, and a spring between each point and the point before and after the corresponding point on the other string (see Fig. 10). This criss-cross arrangement of springs makes each plate quite rigid. The separation between the strings which make up a plate is one mesh width h. This helps separate the flow of interest in the space between the plates from the flow outside the plates. Each immersed boundary point on a wall string is also connected by a spring to a corresponding "tether" point. The tether points for the bottom plate are kept fixed in space to anchor this plate. The tether points for the top wall can be moved to the right with a prescribed speed v. When this is done, the springs between the moving tether points and the immersed boundary points on the top plate generate forces which push the fluid near this plate to the right. All of the spring forces are transmitted to the nearby fluid and thus define the force density term $\mathbf{f}^{ib}$ in Eq. (48) above.

We choose T and use it in (54) to determine E initially, move the top wall at constant speed v until the fluid motion reaches steady state, and then release the top wall from its tether points to see the rebound of the composite material. A marker on the top wall is traced to measure the displacement of the wall. We also sum the spring forces exerted on the tether points of the bottom plate. This is the force needed to hold this plate still when it is pulled on by the motion of the platelet composite and so it can be used to measure the shear stress (σ) on the bottom plate.

We performed a series of experiments in which different times were allowed for link formation before motion began: $T_1 = 0.15625$, $T_2 = 0.3125$, and $T_\infty = \infty$. For each T, we did a set of calculations in which the top wall was moved at speed $v = 0.1, 0.2, 0.4, 0.8,$ or 1.0. Figure 11 shows the shear stress on the bottom wall at steady state versus the shear rate $\gamma = v/L$. We see that the stress increases as the shear rate is increased. In the special case in which the interplatelet link stiffness $K(|\mathbf{v}|) = 0$, the composite material between the


FIG. 10. Two strings of immersed boundary points and a set of elastic springs form a plate.
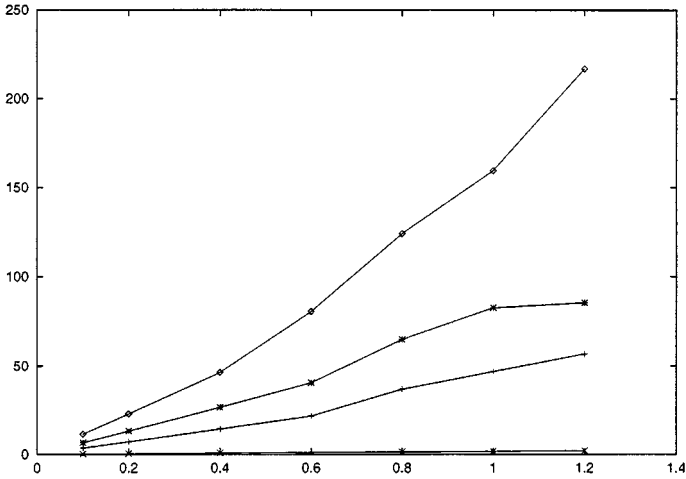
FIG. 11. Shear stress on the bottom wall at steady state for different link formation times. Here curves are $\times$, fluid only; $+$, T_1; $*$, T_2; and $\diamond$, T_∞.

plates should behave as a Newtonian fluid. That this holds for the calculations is shown by the linear plot in Fig. 12.

Curves showing the horizontal displacement of the top wall versus t for different speeds v are displayed in Fig. 13. The curves show that, for these experiments in which no link formation or breaking was allowed after the flow began, the material "remembers" its original configuration and recoils when the top wall is released from its tethers. Over several damped oscillations the displacement drops towards 0. The damping is caused by the fluid viscosity. The overall recoil is similar for all T and v. For fixed T, larger v lead to larger displacements, and larger amplitude oscillations during recoil. The frequency of the oscillations is approximately constant for each T, but increases with higher T. This is because larger T allows more links to be formed before the motion begins and that makes the material stiffer. These results show that under the conditions (without new link
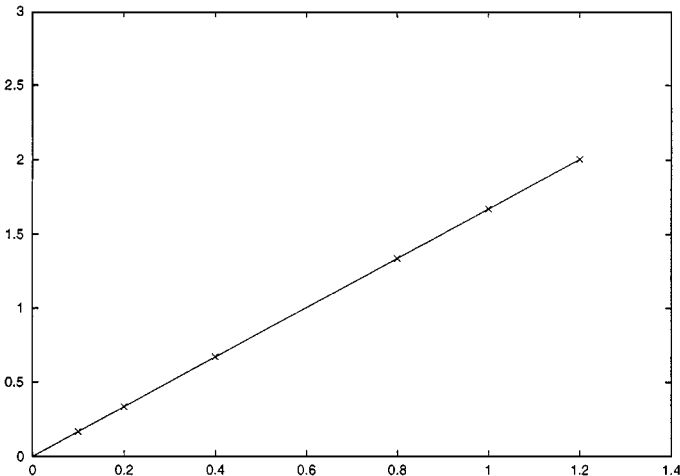
FIG. 12. Shear stress on the bottom wall at steady state with the fluid only.
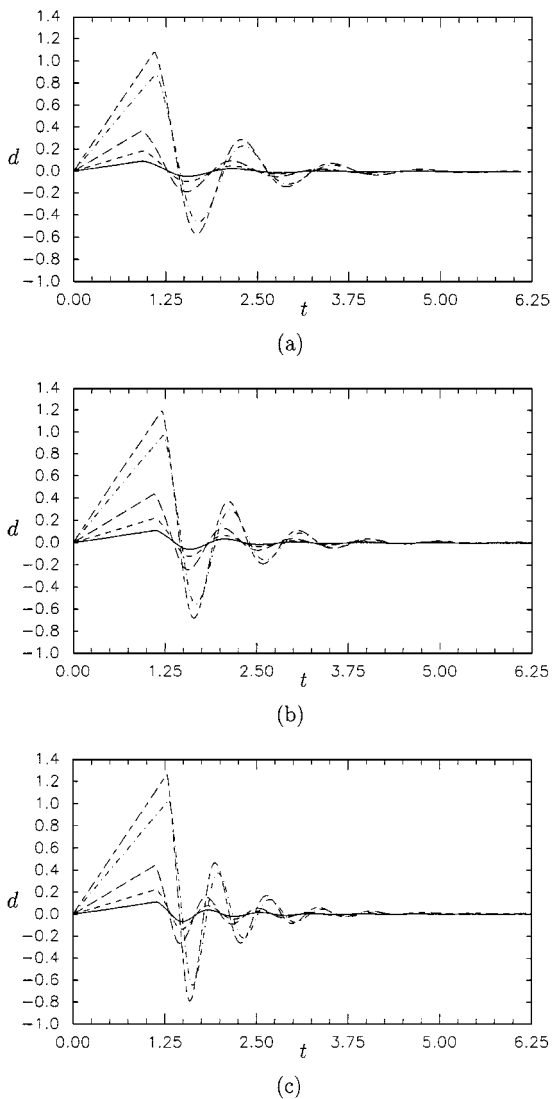
FIG. 13. Displacement of top wall with different v: $v = 0.1, 0.2, 0.4, 0.8$, and 1.0 from solid line up to long-short dashed line. Parts (a), (b), and (c) represent the initial link formation times T_1, T_2, and T_∞, respectively.

formation or breaking) of these experiments, the aggregate composite material behaves as a "viscoelastic" solid.

6. CONCLUSION AND FUTURE WORK

A robust numerical scheme has been assembled for simulating the behavior of Fogelson's continuum models of platelet aggregation. These involve multidimensional high-resolution finite difference schemes for advective transport, ADI schemes for diffusive transport, and a new hybrid finite difference and spectral method for the models' elastic link transport equation. Importantly, the new methods allow the rate β at which links break to depend on the strain on the link.

We have begun to investigate the effects that different assumptions about the bond breaking rate and the bond force function have on the dynamic behavior of aggregates in an elongational flow. From the computational experiments, we could see the competition between new chemically induced activation of platelets and link formation on the one hand and shear-induced link breaking on the other hand. In a certain situation and for certain parameter values, the aggregate broke into two portions. This helps us to establish a numerical experiment in which to explore the medically important embolization process. We have also begun experiments to explore the mechanical properties of the aggregates in the continuum models, as functions of kinetic and mechanical parameters and of the conditions under which the aggregates formed.

In order to carry out a wide range of numerical experiments on the models, it will be helpful to improve further on the computational efficiency of the method. In the simulations to date, we noted that the bond-density function E is often 0 over much of the domain (in **x**-space), and varies slowly over another large part of the domain. The steep gradients are highly localized in regions that change with time. We are exploring the use of adaptive mesh refinement algorithms [4, 3, 2, 14, 5] in the **x**- and **v**-planes for the E equation to concentrate the computational effort in the most needed regions to yield well-resolved results for much less computational work.

It is also possible to use parallel computation to speed the calculations. Because of the explicit time differencing used in the most expensive part of the calculation (the solution of Eq. (6)), and because in **x**-space the stencil of the scheme for Eq. (6) is very local, parallel solution of this equation should be fairly straightforward and effective.

The tools developed in this paper and the extensions just mentioned will allow us to investigate much more systematically the mechanical properties of the platelet composite material and will play a major role in studying new forms of the aggregation models which include platelet-wall interactions [10].

REFERENCES

1. J. B. Bell and D. L. Marcus, A second-order projection method for variable-density flows, *J. Comput. Phys.* **101**, 334 (1992).

2. M. J. Berger, Data structures for adaptive grid generation, *SIAM J. Sci. Stat. Comput.* **7**, 904 (1986).

3. M. J. Berger and A. Jameson, Automatic adaptive grid refinement for the euler equations, *AIAA J.* **23**, 561 (1985).

4. M. J. Berger and J. Oliger, Adaptive mesh refinement for hyperbolic partial differential equations, *J. Comput. Phys.* **53**, 484 (1984).

5. J. Bolstad, *An Adaptive Finite Difference Method for Hyperbolic Systems in One Space Dimension*, Ph.D. thesis, Computer Science Department, Stanford University, 1982.

6. G. V. R. Born, Adenosine diphosphate as a mediator of platelet aggregation in vivo, in *Mechanisms of Stimulus-Response Coupling in Platelets*, edited by J. Westwick, M. F. Scully, D. E. MacIntyre, and V. V. Kakkar, Advances in Experimental Medicine and Biology (Plenum, New York, 1985), Vol. 192, p. 399.

7. C. Canuto, M. Y. Hussaini, A. Quarteroni, and T. A. Zang, *Spectral Methods in Fluid Dynamics* (Springer-Verlag, New York, 1988).

8. A. J. Chorin, Numerical solution of the Navier–Stokes equations, *Math. Comp.* **22**, 745 (1968).

9. P. Colella, Multidimensional upwind methods for hyperbolic conservation laws, *J. Comput. Phys.* **87**, 171 (1990).

10. A. L. Fogelson, Platelet-wall interactions in continuum models of platelet aggregation, submitted.

11. A. L. Fogelson, Continuum models of platelet aggregation: Formulation and mechanical properties, *SIAM J. Appl. Math.* **52**, 1089 (1992).

12. A. L. Fogelson, Continuum models of platelet aggregation: Mechanical properties and chemically-induced phase transitions, in *Fluid Dynamics in Biology*, edited by A. Y. Cheer and C. P. van Dam, Contemporary Mathematics Series (Amer. Math. Soc., Providence, RI, 1993), p. 279.

13. D. Gottlieb and S. A. Orszag, *Numerical Analysis of Spectral Methods: Theory and Applications*, 5th ed. (SIAM-CBMS, Philadelphia, PA, 1977).

14. W. Gropp, A test of moving mesh refinement for 2-d scalr hyperbolic problems, *SIAM J. Sci. Stat. Comput.* **1**, 191 (1980).

15. D. H. Hwang, Species variation in platelet aggregation, in *The Platelets: Physiology and Pharmacology*, edited by G. L. Longenecker, Physiologic and Pharmacologic Bases of Drug Therapy (Academic Press, Orlando, FL, 1985), p. 289.

16. J. D. Lambert, *Computational Methods in Ordinary Differential Equations* (Wiley, New York, 1973).

17. R. J. LeVeque, High resolution finite volume methods on arbitrary grids via wave propagation, *J. Comput. Phys.* **78**, 36 (1988).

18. R. J. LeVeque, Simplified multi-dimensional flux limiter methods, in *Numerical Methods for Fluid Dynamics*, edited by M. Baines and K. Morton (Oxford Univ. Press, London, 1993), Vol. 4, p. 175.

19. R. J. LeVeque, CLAWPACK, software package, 1994.

20. R. J. LeVeque, High-resolution conservative algorithms for advection in incompressible flow, *SIAM J. Numer. Anal.* **33**, 627 (1996).

21. A. R. Mitchell and D. F. Griffiths, *The Finite Difference Method in Partial Differential Equations* (Wiley, New York, 1980).

22. J. F. Mustard and M. A. Packham, Factors influencing platelet function: Adhesion, release and aggregation, *Pharmacol. Rev.* **22**, 97 (1970).

23. C. S. Peskin, Numerical analysis of blood flow in the heart, *J. Comput. Phys.* **25**, 220 (1977).

24. A. Szczeklik and J. Musial, Platelets and ischemic heart disease, in *The Platelets: Physiology and Pharmacology*, edited by G. L. Longenecker, Physiologic and Pharmacologic Bases of Drug Therapy (Academic Press, Orlando, FL, 1985), p. 407.